

# Superconductivity, Anomalous Hall Effect, and Stripe Order in Rhombohedral Hexalayer Graphene

Erin Morissette<sup>1,\*</sup>, Peiyu Qin<sup>1,\*</sup>, Hai-Tian Wu<sup>1</sup>, Naiyuan J. Zhang<sup>1</sup>, K. Watanabe<sup>2</sup>, T. Taniguchi<sup>3</sup>, and J.I.A. Li<sup>1†</sup>

<sup>1</sup>*Department of Physics, Brown University, Providence, RI 02912, USA*

<sup>2</sup>*Research Center for Functional Materials, National Institute for Materials Science, 1-1 Namiki, Tsukuba 305-0044, Japan and*

<sup>3</sup>*International Center for Materials Nanoarchitectonics,*

*National Institute for Materials Science, 1-1 Namiki, Tsukuba 305-0044, Japan*

(Dated: April 17, 2025)

Unconventional superconducting phases are distinguished by broken symmetries in their order parameters. Here, we report the discovery of an exotic superconducting phase in rhombohedral hexalayer graphene at high displacement fields, marked by its coexistence with both a stripe charge order and the anomalous Hall effect. In angle-resolved transport measurements, the onset of stripe order is manifested as thermally activated insulating behavior along one axis, with highly conductive transport along the orthogonal direction. Upon cooling, superconductivity emerges exclusively along the high-conductivity axis, forming one-dimensional-like superconducting channels. This anisotropic superconducting phase exhibits multiple first-order hysteretic transitions. Pronounced thermal hysteresis between warming and cooling across the superconducting transition suggests a melting transition of the underlying stripe phase. Additionally, magnetic-field-induced switching—similar to phenomena reported in tetra- and pentalayer graphene—supports the chiral nature of the superconducting state. Together, these findings identify a previously unrecognized quantum phase: a chiral superconductor embedded within a stripe Hall crystal.

The superfluid A-phase of  $^3\text{He}$ , which emerges at ultralow temperatures around 2 mK in the strong-coupling regime, provides a prototypical example of chiral superconductivity [1]. In this remarkable state, Cooper pairing occurs with non-zero angular momentum, allowing the phase to be simultaneously understood as a  $p$ -wave superconductor and an orbital ferromagnet [2, 3]. This duality is manifested in a net magnetization associated with the angular momentum of the Cooper pairs. When confined to a slab geometry, spatial confinement aligns the orbital magnetic moments perpendicular to the plane, producing two degenerate configurations with magnetic moments pointing either up or down [4]. Most remarkably, applying an out-of-plane magnetic field drives a transition between these configurations by reversing the direction of the magnetic moment—a process that manifests in the transport response of moving electron bubbles. This distinctive transport signature provides direct evidence of

the chiral nature of the superfluid A-phase of  $^3\text{He}$ .

Despite decades of effort to identify a chiral superconductor in a solid-state platform, the superfluid A-phase of  $^3\text{He}$  remained the only known example until recently. A promising candidate has now emerged in the superconducting phases of tetra- and pentalayer rhombohedral graphene [5–11]. In these systems, the Cooper pairing instability appears to be intimately linked to orbital ferromagnetism. The resulting superconducting phase exhibits magnetic-field-driven switching between distinct ground states—closely resembling the hallmark behavior of the  $^3\text{He}$  A-phase [5].

Unlike the fluid phase of  $^3\text{He}$ , where chiral order emerges in relative isolation, the low-temperature phase diagrams of two-dimensional (2D) electron systems—particularly those governed by strong Coulomb interactions—often host a rich interplay of coexisting and competing orders [12–16]. Among these, multilayer graphene with rhombohedral stacking has emerged as a particularly fertile platform, where the emergence of superconductivity is intertwined with a broad spectrum of electronic orders [5, 17–20]. Notably, recent experiments have revealed that the onset of time-reversal symmetry breaking (TRSB) in rhombohedral multilayer graphene is intimately linked to spontaneous rotational symmetry breaking [21]. This observation raises the compelling possibility that the chiral superconducting state in these systems intrinsically features broken rotational symmetry—a hypothesis we investigate in this work.

To investigate this possibility, we leverage recent advances in angle-resolved transport techniques [21–27], which offer powerful tools for probing how intertwined electronic orders emerge and evolve alongside superconductivity. Applying these methods to rhombohedral hexalayer graphene, we uncover a prominent stripe charge order that coexists with both superconductivity and the anomalous Hall effect.

The low-temperature phase diagram of rhombohedral hexalayer graphene hosts three distinct superconducting pockets, as shown in Fig. 1a, labeled  $SCi$ ,  $SCii$ , and  $SCiii$  in Fig. 1b. Their superconducting transitions are evident in the  $R$ – $T$  characteristics displayed in Fig. 1c. While all three pockets are proximate to regimes of orbital ferromagnetism,  $SCi$  emerges from a valley-polarized metallic phase and uniquely exhibits a pronounced coexistence

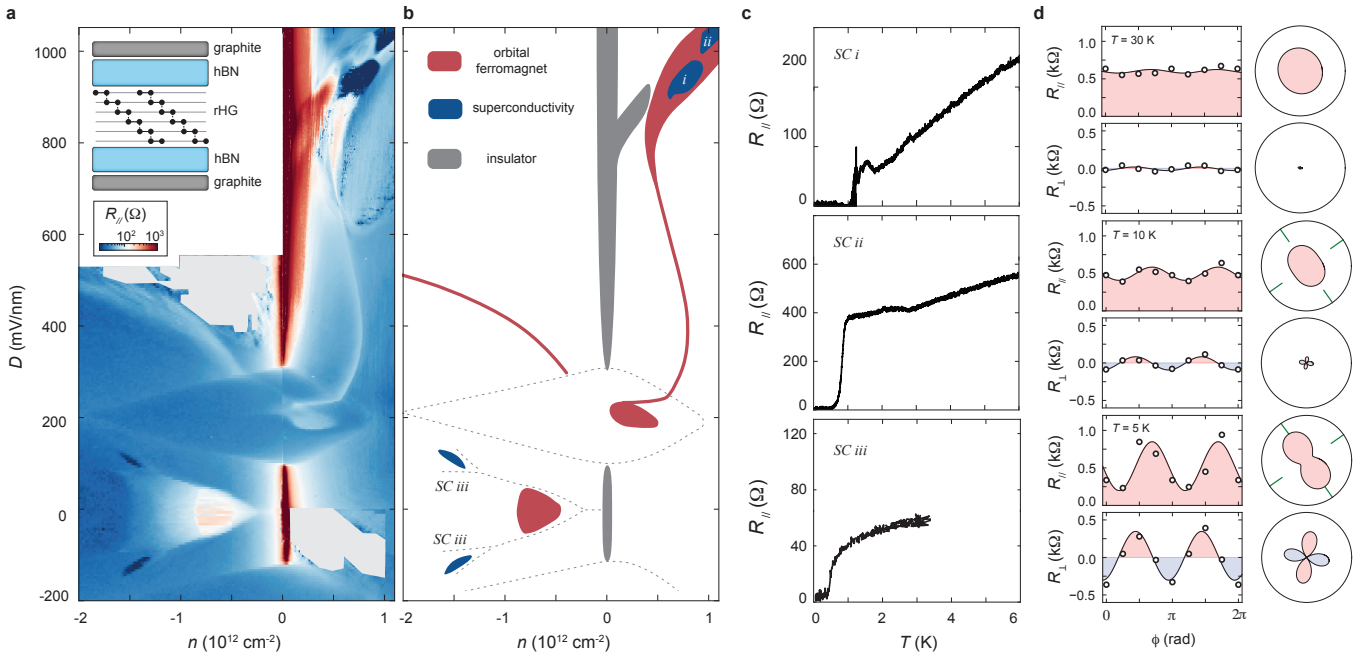


**FIG. 1. Low-temperature phase diagram of rhombohedral hexalayer graphene.** (a) Color-scale map of the longitudinal resistance  $R_{\parallel}$ , measured at  $T = 40$  mK and  $B = 0$ , as a function of carrier density  $n$  and displacement field  $D$ . (b) Schematic illustrating the emergent orders derived from panel (a), with superconducting pockets labeled  $SC\ i$ ,  $SC\ ii$ , and  $SC\ iii$ . (c)  $R$ - $T$  curves measured from  $SC\ i$  (top),  $SC\ ii$  (middle), and  $SC\ iii$  (bottom). (d) Angle-resolved transport measured at  $T = 30$  K (top), 20 K (middle), and 10 K (bottom). Solid curves denote the best fits using Eqs. (M1) and (M2).

with stripe charge order (see Fig. M1 and Fig. M2). Accordingly, our study focuses on the unconventional properties of the  $SCi$  phase. For completeness, we also comment on the angular transport behavior observed in  $SCii$  and  $SCiii$  in the Methods section.

We begin by examining the transport properties in the metallic regime above the superconducting transition temperature. The sample geometry and angle-resolved measurement setup have been described in detail in previous studies [21, 25–27]. Figure 1d presents the angular dependence of both the longitudinal and transverse resistances,  $R_{\parallel}$  and  $R_{\perp}$ , measured at carrier density  $n$  and displacement field  $D$  values corresponding to the  $SCi$  regime. At  $T = 30$  K, the transport response is nearly isotropic, but as the temperature decreases, a pronounced anisotropy emerges. As shown in Fig. 1d, the principal axes of transport anisotropy—defined by the directions of maximum and minimum resistance—are aligned along  $\phi = 45^\circ$  and  $135^\circ$ , respectively.

Figure 2a shows  $R_{\parallel}$  as a function of temperature, measured at various angles  $\phi$ . The maximum and minimum resistance values,  $R_{\max}$  and  $R_{\min}$ , are observed when current is applied along the principal axes of the transport anisotropy. The increasing divergence between  $R_{\max}$  and  $R_{\min}$  at low temperatures signals the emergence of extreme transport anisotropy.

We define the anisotropy parameter as  $\xi = (R_{\max} - R_{\min})/(R_{\max} + R_{\min})$ , which is equivalent to  $\Delta R/R_0$  in

Eq. M1–M2 [21, 24, 27]. The dashed line in Fig. 2b represents the best fit of the temperature dependence of  $\xi$  to the Curie–Weiss law. The excellent agreement between the experimental data and the Curie–Weiss fit indicates a thermodynamic transition driven by nematic instabilities [28–30].

Notably, transport along the principal axis of maximum resistivity (i.e., minimum conductivity) exhibits thermally activated insulating behavior, as shown in the inset of Fig. 2b. A linear fit to the Arrhenius plot yields an energy gap of approximately  $\Delta \approx 4.5$  K. In stark contrast, charge transport along the orthogonal axis remains highly conductive. The emergence of activated behavior along only one direction is an unprecedented observation. It points to the formation of an exotic electronic order that goes beyond conventional nematicity. We propose that our findings arise from the formation of a stripe charge order at low temperature [31–36], with the easy axis aligned near  $\phi = 45^\circ$  (indicated by the blue arrow in the inset of Fig. 2b).

Central to our observation is the profound impact of stripe charge order on superconducting transport. As superconductivity emerges at low temperatures, its transport response inherits the spatial anisotropy imposed by the stripe order. When current is applied along the stripe orientation, the superconducting transition temperature  $T_c$  reaches a maximum near 1 K. In contrast, when the current is misaligned by  $45^\circ$ —as shown in the inset of

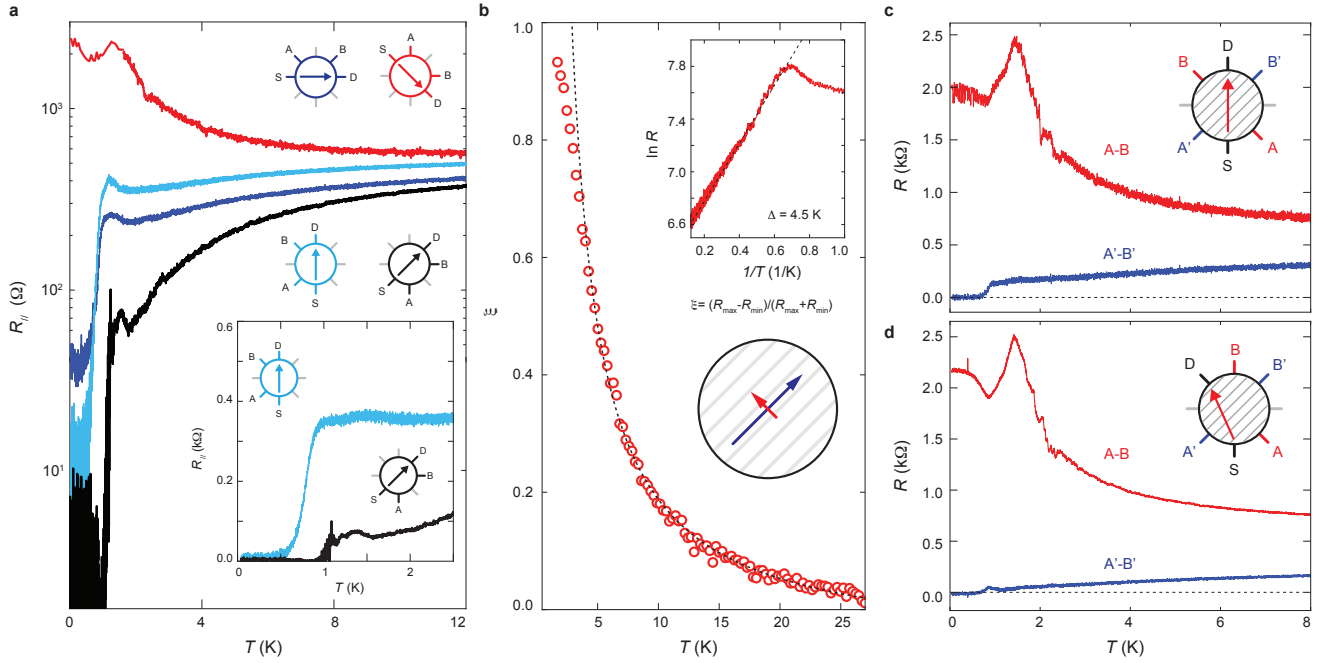


**FIG. 2. The stripe order and extreme anisotropy in superconducting transport.** (a) Resistance versus temperature,  $R-T$ , measured with current flowing along different directions relative to the stripe order. The inset shows  $R_{\parallel}$ , on a linear scale, for current applied parallel (black trace) and slightly misaligned (light blue) from the principal axis. (b) Temperature dependence of the transport anisotropy, defined as  $\xi = (R_{\max} - R_{\min})/(R_{\max} + R_{\min})$ , which follows a Curie–Weiss form (black dashed line). Top inset: Arrhenius plot of the hard-axis  $R-T$  curve ( $\phi = 135^\circ$ ), revealing a thermally activated gap  $\Delta \approx 4.5$  K. Bottom inset: schematic of the stripe charge order, indicating the “easy” (high conductivity) axis at  $\phi = 225^\circ$  and the “hard” (insulating) axis at  $\phi = 135^\circ$ . (c), (d)  $R-T$  traces measured in the respective configurations indicated by the insets. When the current flow is partially misaligned with the stripes, the measured resistance is highly sensitive to whether the voltage leads lie along or perpendicular to the stripe direction. As a result, the onset of superconductivity causes negligible voltage drops between leads aligned with the stripes, while leads oriented perpendicular to the stripes still display insulating behavior. All measurements are performed at  $n = 0.8 \times 10^{12} \text{ cm}^{-2}$  and  $D = 958 \text{ mV/nm}$ , inside  $SC\ i$ .

Fig. 2a— $T_c$  is suppressed by nearly a factor of two. A more dramatic suppression occurs when current is applied transverse to the stripe orientation, along  $\phi = 135^\circ$ , where insulating behavior persists down to the base temperature of the dilution refrigerator ( $T = 30$  mK). This extreme anisotropy is reminiscent of quantum Hall stripe phases [33–36], though distinguished here by the emergence of superconductivity along the stripe direction.

Crucially, the extreme transport anisotropy we observe is robust against variations in measurement configuration. For example, Fig. 2c shows an alternative setup with current applied along  $\phi = 90^\circ$ . In this arrangement, voltage probes positioned perpendicular to the stripe direction (A, B) display a low-temperature insulating response, while probes aligned along the stripes (A', B') exhibit diminishing resistance as temperature decreases. For simplicity, we refer to this setup as the *cross configuration*. A similar observation is made using different source–drain and voltage contact pairs, as shown in Fig. 2d: once again, the transport response reveals insulating behavior transverse to the stripes and dissipationless behavior along them.

Additional configurations in Fig. M10 and Fig. M11 further demonstrate that whether the response is insulating or superconducting is solely determined by the orientation relative to the stripe order—ruling out poor electrical contacts as the cause. These observations confirm that the coexistence of insulating and superconducting responses originates from the stripe formation, rather than from artifacts related to specific contact geometry.

In the following, we report a rich array of hysteretic behaviors in transport measurements that underscore the remarkable coexistence of superconductivity, stripe charge order, and the anomalous Hall effect.

Most notably, the emergence of stripe order is accompanied by a crystalline phase transition, evidenced by a first-order melting process with pronounced supercooling and superheating. This transition manifests as temperature-driven hysteresis in the insulating response when current is applied perpendicular to the stripe direction. As shown in Figs. 3c–d, both  $R_{\parallel}$  and  $R_{\perp}$  measured along  $\phi = 135^\circ$  exhibit clear hysteresis loops during controlled warming and cooling (see Methods for details). Importantly, the magnitude and asymmetry of

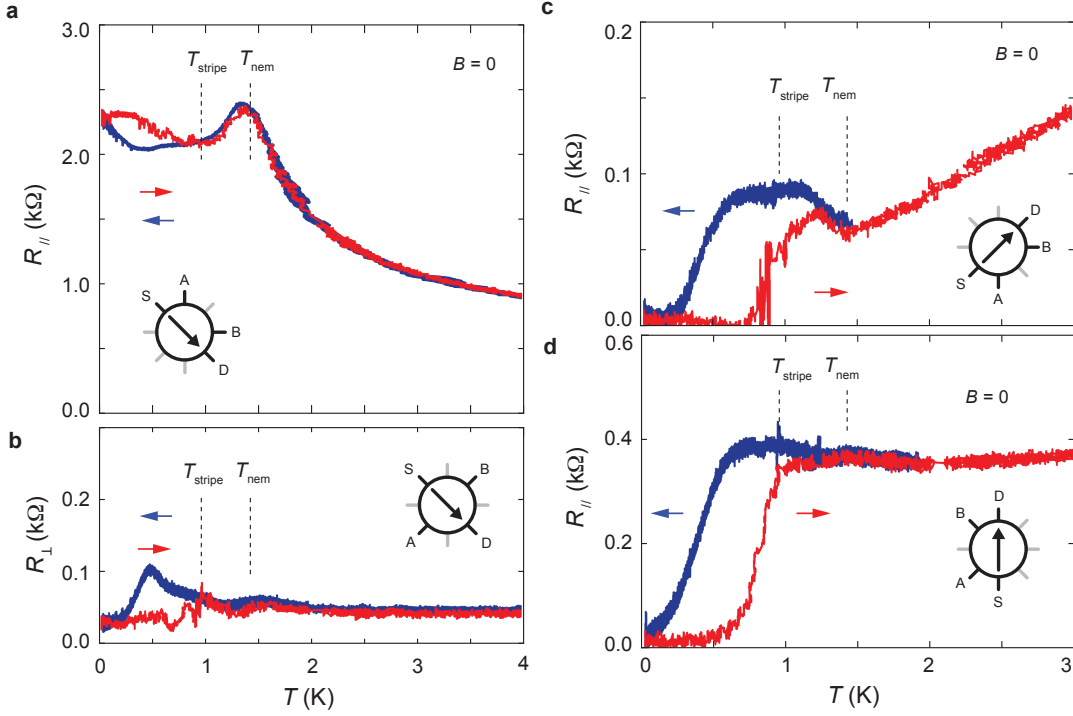


**FIG. 3. Temperature-driven hysteretic transitions and stripe melting.** (c–d) Temperature sweep of (c)  $R_{\parallel}$  and (d)  $R_{\perp}$  measured during both warming and cooling cycles with current applied perpendicular to the stripe orientation at  $\phi = 135^\circ$ . (e–f)  $R_{\parallel}$  versus  $T$  measured during both warming and cooling cycles along (e)  $\phi = 225^\circ$  and (f)  $270^\circ$ , displaying prominent hysteresis in the superconducting transition. Measurements are performed at  $D = 958$  mV/nm and  $n = 8 \times 10^{12}$  cm $^{-2}$ .

these loops—such as the resistance peak in  $R_{\perp}$  observed only during cooling—offer crucial confirmation for their intrinsic origin and rule out experimental artifacts.

The hysteretic  $R$ – $T$  curves also offer insight into the characteristic temperature associated with stripe formation. As shown in Figs. 3a–b, we define the stripe melting temperature ( $T_{\text{stripe}}$ ) as the onset of temperature-driven hysteresis in the insulating response measured perpendicular to the stripe direction. In this context, the resistance cusp observed in  $R_{\parallel}$  (Fig. 3a) reflects a thermodynamic transition driven by nematic instability, without involving crystalline order.

Remarkably,  $T_{\text{stripe}}$  coincides with the onset of superconductivity when current flows along the stripe direction (Fig. 3c), highlighting a direct link between superconductivity and stripe formation.

Even more striking is the observation of hysteresis across the superconducting transition itself. As shown in Figs. 3c–d, the superconducting transition—defined by the vanishing of  $R_{\parallel}$ —occurs at a significantly lower temperature during cooling, indicative of a first-order transition.

The presence of hysteresis in the superconducting transition is highly unusual. First-order transitions in superconductors typically occur between distinct superconducting phases with different order parameters, such as the A- and B-phases of superfluid  $^3\text{He}$  [1]. In contrast,

transitions between superconducting and normal states are generally expected to be continuous and second-order. In our system, however, several plausible mechanisms may lead to a first-order superconducting transition:

- (i) The melting of the stripe charge order is itself a first-order transition. Therefore, the hysteresis observed in the superconducting transition may naturally result from the supercooling and superheating associated with stripe melting.
- (ii) The superconducting transition temperature ( $T_c$ ) is extremely sensitive to the relative orientation between the applied current and the stripe direction. In this scenario, the hysteresis arises from subtle changes in stripe orientation induced either by thermal cycling above  $T_{\text{stripe}}$  or by current-direction switching during the measurement sequence.
- (iii) There may exist a temperature-driven transition between two distinct superconducting phases, analogous to the A- and B-phases of superfluid  $^3\text{He}$ . Supercooling and superheating across such a first-order transition would naturally lead to the observed pronounced hysteresis [37–39].

Each of these scenarios highlights the complex and intertwined nature of stripe order and superconductivity

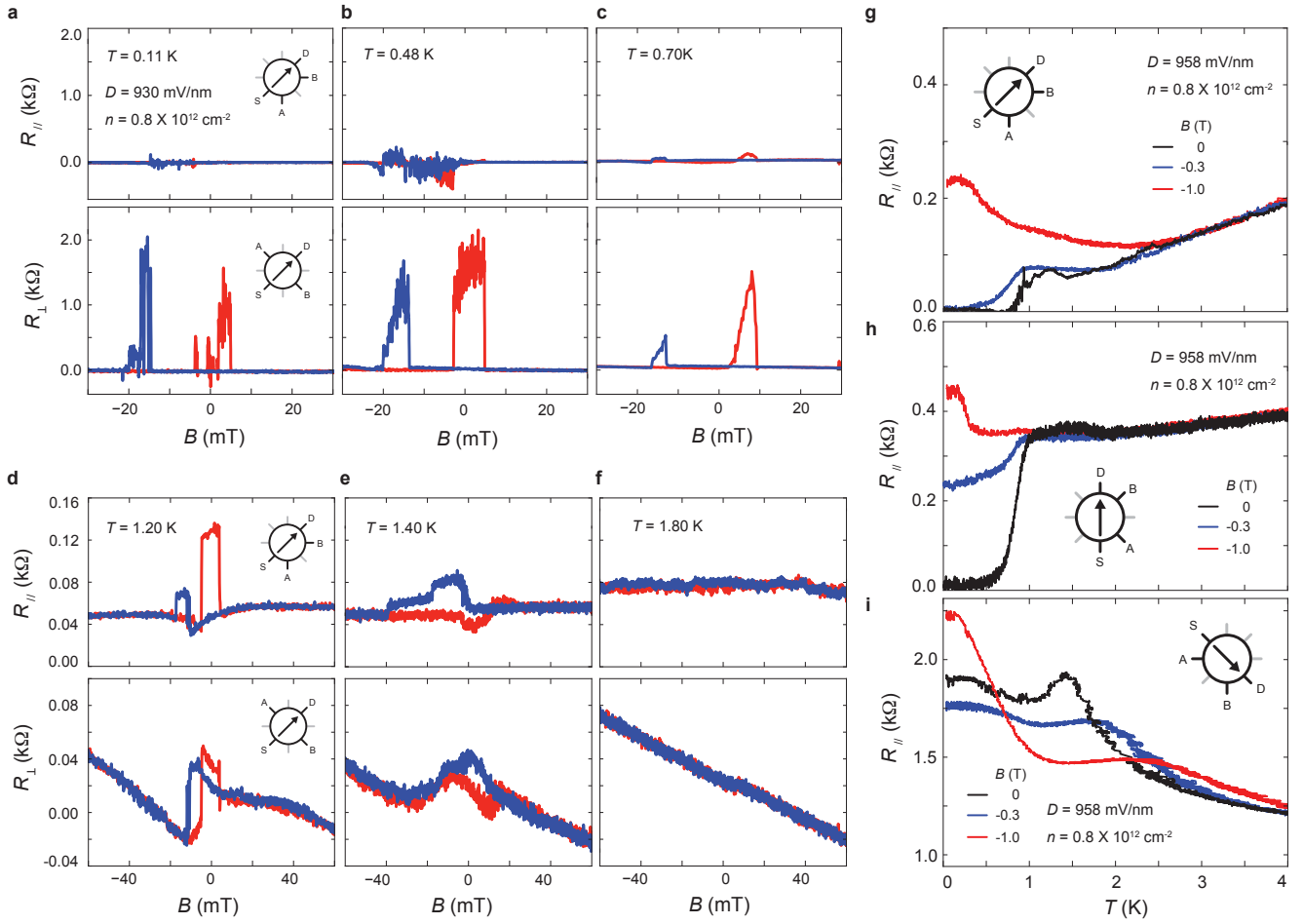


FIG. 4. **Magnetic-field-driven hysteretic transitions and chiral superconductivity.** (a-f)  $R_{\parallel}$  (top panels) and  $R_{\perp}$  (bottom panels) as a function of out-of-plane magnetic field  $B$  measured with current flowing parallel to the stripe direction at (a)  $T = 0.11$  K, (b)  $0.48$  K, (c)  $0.81$  K, (d)  $1.40$  K, and (e)  $1.80$  K. Measurements in (a-f) are performed at  $D = 930$  mV/nm and  $n = 8 \times 10^{12} \text{ cm}^{-2}$ . (g-i)  $R_{\parallel}$  as a function of  $T$  measured at different values of out-of-plane  $B$ -field and current flow directions.

in this system, and calls for further investigation into the microscopic origin of the hysteretic superconducting transition.

Next, we show that the superconducting phase undergoes hysteretic transitions driven by an out-of-plane magnetic field ( $B_{\perp}$ ), indicative of a first-order transition between degenerate order-parameter configurations—closely analogous to the A-phase of superfluid  $^3\text{He}$ , a prototypical chiral superconductor [4]. Figures 4a–c present superconducting transport responses with current flowing parallel to the stripe direction, measured as  $B_{\perp}$  is swept back and forth at different temperatures. Both  $R_{\parallel}$  and  $R_{\perp}$  remain vanishingly small across most of the  $B$  range, while field-driven reversals of the underlying valley polarization are marked by prominent peaks in  $R_{\perp}$ .

Such magnetic-field–driven switching is consistent with recent observations in rhombohedral tetra- and pentalayer graphene [5], and offers strong support for the chiral

nature of the superconducting phase.

While the field-driven reversal of valley polarization manifests as pronounced peaks in  $R_{\perp}$ ,  $R_{\parallel}$  remains largely featureless below the stripe formation temperature ( $T < 0.8$  K). It has been proposed that a resistive signal in the superconducting phase arises when a domain boundary lies between voltage probes [5]. In this context, the contrasting behavior between  $R_{\parallel}$  and  $R_{\perp}$  may reflect a tendency for domain boundaries to align preferentially along the stripe direction. As temperature increases, field-driven reversal becomes visible in both  $R_{\parallel}$  and  $R_{\perp}$  around  $T = 0.8$  K, consistent with the stripe melting temperature identified in Fig. 3. In this regime, domain boundaries are no longer pinned to the stripe orientation.

The magnetic-field–driven hysteresis loop persists up to  $T = 1.4$  K, indicating that spontaneous valley polarization is a more robust order than both superconductivity and stripe formation. Intriguingly, the onset of the anomalous Hall effect coincides with the nematic

transition temperature  $T_{\text{nem}}$  (Fig. 3). This connection is further evidenced by the overlapping phase space where extreme transport anisotropy and the anomalous Hall effect coexist, as shown in Fig. M1. A similar correlation has been observed in the multiferroic phase of rhombohedral hexalayer graphene near zero displacement field ( $D \approx 0$ ) [21]. These observations point to a potential common origin for time-reversal and rotational symmetry breaking.

Such a shared origin could naturally arise from Coulomb-driven instabilities of a valley-polarized Fermi surface, which favor spontaneous condensation in momentum space [6, 40–43]. Momentum-space condensation has been widely explored in the context of multilayer graphene systems [26, 44]. From a momentum-polarized parent state, the emergence of superconductivity permits finite-momentum Cooper pairing—a scenario directly linked to the superconducting diode effect at zero magnetic field [45–47]. With its distinct combination of broken symmetries, the  $SC\ i$  phase presents an ideal platform to explore nonreciprocal superconducting transport. While a full study of the diode effect lies beyond the scope of this work, we note that prior zero-field diode reports also involved coexisting superconductivity and a density wave [45]. However, in those cases, the angular symmetry of the density wave could not be resolved due to the constraints of Hall-bar geometries.

The existence of valley polarization above the superconducting transition also distinguishes this system from the A-phase of superfluid  $^3\text{He}$ , where the normal fluid phase preserves time-reversal symmetry.

Taken together, our observations reveal a remarkable and intricate interplay among multiple emergent electronic orders. Above the superconducting transition temperature, the anomalous Hall effect emerges concurrently with pronounced transport anisotropy at the nematic transition  $T_{\text{nem}}$ , highlighting a metallic phase characterized by spontaneous momentum-space condensation. In the low-temperature regime, magnetic-field-driven hysteretic switching between degenerate superconducting states strongly supports the chiral nature of the superconducting order parameter [5]. The simultaneous onset of superconductivity and stripe charge order naturally leads to a spatial modulation of the superconducting gap, establishing this system as a promising platform for realizing pair density wave states [48]. Furthermore, the coexistence of stripe order and the anomalous Hall effect provides compelling experimental evidence for a stripy anomalous Hall crystal [49–54].

Despite its coexistence and competition with stripe order, the superconducting transition temperature ( $T_c$ ) in rhombohedral hexalayer graphene is significantly higher than values reported for other rhombohedral multilayer graphene systems [5, 18, 19]. This enhanced  $T_c$  may arise from stronger Coulomb interactions associated with the flatter bands in hexalayer graphene, as suggested by

both theoretical predictions and experimental observations [55–57].

Furthermore, previous studies of rhombohedral pentalayer graphene aligned with hexagonal boron nitride (hBN) have also hinted at the presence of an anomalous Hall crystal phase [58, 59]. Our observation of stripe order coexisting with the anomalous Hall effect within a similar region of the  $n$ - $D$  phase diagram suggests that stripe formation may represent a universal ordering tendency in rhombohedral multilayer graphene under strong displacement fields.

An outstanding signature of the superconducting phase in rhombohedral tetra- and pentalayer graphene is its remarkable stability against large out-of-plane magnetic fields ( $B_\perp$ ) [5]. In rhombohedral hexalayer graphene, however, this stability depends sensitively on the orientation of the applied current relative to the stripe direction. When current flows along the stripe orientation,  $R$ - $T$  curves exhibit a sharp superconducting transition that persists even under a substantial out-of-plane magnetic field of  $B_\perp = 0.3$  T (Fig. 4h). As illustrated in Fig. M12,  $R_{\parallel}$  measured along the stripe direction remains nearly zero up to approximately  $B_\perp = 0.75$  T.

In contrast, when current is applied along  $\phi = 270^\circ$ —misaligned by approximately  $45^\circ$  from the stripe direction—the application of  $B_\perp = -0.3$  T fully suppresses dissipationless superconducting transport at low temperatures (Fig. 4h). Under this field, superconductivity is observed only when the current is perfectly aligned with the stripe orientation. When  $B_\perp$  is further increased to  $-1$  T, superconductivity is completely suppressed, independent of the current direction (Fig. 4i). In this high-field regime, the  $R$ - $T$  curves display an upturn at low temperatures, consistent with the reemergence of a stripe-ordered insulating phase.

Lastly, we comment on the angular interplay between superconductivity and the metallic phase. In  $SC\ i$ , the most robust superconducting response consistently occurs along the direction of maximum conductivity (minimum resistivity) observed in the metallic phase above  $T_c$ . While  $SC\ ii$  and  $SC\ iii$  do not exhibit the extreme anisotropy seen in  $SC\ i$ , they share the same angular interplay between superconducting and metallic transport (see Fig. M13). This behavior stands in stark contrast to recent findings in magic-angle twisted trilayer graphene [27], where superconductivity is strongest along the direction of minimum conductivity (maximum resistivity) in the normal state. These observations establish a fundamental distinction between the superconducting phases in rhombohedral hexalayer graphene and those previously reported in magic-angle graphene moiré systems [60–65].

## ACKNOWLEDGMENTS

J.I.A.L. wishes to thank Oskar Vafek for continued support and theoretical guidance in developing the novel scheme of angle-resolved transport measurement. J.I.A.L. also acknowledges helpful discussions with Sankar Das Sarma, Dima Feldman, Aaron Hui, Mathias Scheurer, Chunli Huang, and Boris Shklovskii. E.M. and J.I.A.L. acknowledge support from U.S. National Science Foundation under Award DMR-2143384. J.I.A.L. acknowledge partial support from the Air Force Office of Scientific Research. K.W. and T.T. acknowledge support from the JSPS KAKENHI (Grant Numbers 21H05233 and 23H02052) and World Premier International Research Center Initiative (WPI), MEXT, Japan. Part of this work was enabled by the use of pycan ([github.com/sandialabs/pycan](https://github.com/sandialabs/pycan)), scientific measurement software made available by the Center for Integrated Nanotechnologies, an Office of Science User Facility operated for the U.S. Department of Energy.

- [17] H. Zhou, T. Xie, A. Ghazaryan, T. Holder, J. R. Ehrets, E. M. Spanton, T. Taniguchi, K. Watanabe, E. Berg, M. Serbyn, *et al.*, *Nature* **598**, 429 (2021).
- [18] H. Zhou, T. Xie, T. Taniguchi, K. Watanabe, and A. F. Young, *Nature* **598**, 434 (2021).
- [19] H. Zhou, L. Holleis, Y. Saito, L. Cohen, W. Huynh, C. L. Patterson, F. Yang, T. Taniguchi, K. Watanabe, and A. F. Young, *Science* **375**, 774 (2022).
- [20] Y. Choi, Y. Choi, M. Valentini, C. L. Patterson, L. F. Holleis, O. I. Sheekey, H. Stoyanov, X. Cheng, T. Taniguchi, K. Watanabe, *et al.*, *Nature* **1** (2025).
- [21] E. Morissette, P. Qin, K. Watanabe, T. Taniguchi, and J. Li, arXiv preprint arXiv:2503.09954 (2025).
- [22] J. Wu, A. Bollinger, X. He, and I. Božović, *Nature* **547**, 432 (2017).
- [23] J. Wu, H. P. Nair, A. T. Bollinger, X. He, I. Robinson, N. J. Schreiber, K. M. Shen, D. G. Schlom, and I. Božović, *Proceedings of the National Academy of Sciences* **117**, 10654 (2020).
- [24] O. Vafek, *Phys. Rev. Appl.* **20**, 064008 (2023).
- [25] D. V. Chichinadze, N. J. Zhang, J.-X. Lin, X. Wang, K. Watanabe, T. Taniguchi, O. Vafek, and J. Li, arXiv preprint arXiv:2411.11156 (2024).
- [26] N. J. Zhang, J.-X. Lin, D. V. Chichinadze, Y. Wang, K. Watanabe, T. Taniguchi, L. Fu, and J. I. A. Li, *Nature Materials* **23**, 356 (2024).
- [27] N. J. Zhang, P. A. Nosov, O. E. Sommer, Y. Wang, K. Watanabe, T. Taniguchi, E. Khalaf, and J. Li, arXiv preprint arXiv:2503.15767 (2025).
- [28] J.-H. Chu, H.-H. Kuo, J. G. Analytis, and I. R. Fisher, *Science* **337**, 710 (2012).
- [29] R. Fernandes, A. Chubukov, and J. Schmalian, *Nature physics* **10**, 97 (2014).
- [30] A. E. Böhmer, J.-H. Chu, S. Lederer, and M. Yi, *Nature Physics* **18**, 1412 (2022).
- [31] M. M. Fogler, A. A. Koulakov, and B. I. Shklovskii, *Phys. Rev. B* **54**, 1853 (1996).
- [32] A. A. Koulakov, M. M. Fogler, and B. I. Shklovskii, *Phys. Rev. Lett.* **76**, 499 (1996).
- [33] M. Lilly, K. Cooper, J. Eisenstein, L. Pfeiffer, and K. West, *Physical Review Letters* **82**, 394 (1999).
- [34] M. P. Lilly, K. B. Cooper, J. P. Eisenstein, L. N. Pfeiffer, and K. W. West, *Phys. Rev. Lett.* **83**, 824 (1999).
- [35] R. Du, D. Tsui, H. Stormer, L. Pfeiffer, K. Baldwin, and K. West, *Solid State Communications* **109**, 389 (1999).
- [36] W. Pan, R. R. Du, H. L. Stormer, D. C. Tsui, L. N. Pfeiffer, K. W. Baldwin, and K. W. West, *Phys. Rev. Lett.* **83**, 820 (1999).
- [37] P. Schiffer, M. O'keefe, M. Hildreth, H. Fukuyama, and D. Osheroff, *Physical review letters* **69**, 120 (1992).
- [38] P. Schiffer and D. Osheroff, *Reviews of Modern Physics* **67**, 491 (1995).
- [39] Y. Tian, D. Lotnyk, A. Eyal, K. Zhang, N. Zhelev, T. Abhilash, A. Chavez, E. Smith, M. Hindmarsh, J. Saunders, *et al.*, *Nature communications* **14**, 148 (2023).
- [40] Z. Dong, M. Davydova, O. Ogunnaike, and L. Levitov, *Phys. Rev. B* **107**, 075108 (2023).
- [41] J. Jung, M. Polini, and A. H. MacDonald, *Physical Review B* **91**, 155423 (2015).
- [42] C. Huang, T. M. Wolf, W. Qin, N. Wei, I. V. Blinov, and A. H. MacDonald, *Physical Review B* **107**, L121405 (2023).
- [43] I. Mandal and R. M. Fernandes, *Physical Review B* **107**, 125142 (2023).

[44] J.-X. Lin, Y. Wang, N. J. Zhang, K. Watanabe, T. Taniguchi, L. Fu, and J. Li, arXiv preprint arXiv:2302.04261 (2023).

[45] J.-X. Lin, P. Siriviboon, H. D. Scammell, S. Liu, D. Rhodes, K. Watanabe, T. Taniguchi, J. Hone, M. S. Scheurer, and J. Li, *Nature Physics* **18**, 1221 (2022).

[46] H. D. Scammell, J. Li, and M. S. Scheurer, *2D Materials* **9**, 025027 (2022).

[47] N. F. Q. Yuan and L. Fu, arXiv e-prints (2021), [arXiv:2106.01909 \[cond-mat.supr-con\]](https://arxiv.org/abs/2106.01909).

[48] D. F. Agterberg, J. S. Davis, S. D. Edkins, E. Fradkin, D. J. Van Harlingen, S. A. Kivelson, P. A. Lee, L. Radzihovsky, J. M. Tranquada, and Y. Wang, *Annual Review of Condensed Matter Physics* **11**, 231 (2020).

[49] T. Tan and T. Devakul, *Physical Review X* **14**, 041040 (2024).

[50] J. Dong, T. Wang, T. Wang, T. Soejima, M. P. Zaletel, A. Vishwanath, and D. E. Parker, *Physical Review Letters* **133**, 206503 (2024).

[51] T. Soejima, J. Dong, T. Wang, T. Wang, M. P. Zaletel, A. Vishwanath, and D. E. Parker, *Physical Review B* **110**, 205124 (2024).

[52] Z. Dong, A. S. Patri, and T. Senthil, *Phys. Rev. B* **110**, 205130 (2024).

[53] A. S. Patri, Z. Dong, and T. Senthil, *Phys. Rev. B* **110**, 245115 (2024).

[54] Z. Dong, A. S. Patri, and T. Senthil, *Phys. Rev. Lett.* **133**, 206502 (2024).

[55] Y. Zhang, Y.-Y. Zhou, S. Zhang, H. Cai, L.-H. Tong, W.-Y. Liao, R.-J. Zou, S.-M. Xue, Y. Tian, T. Chen, *et al.*, *Nature Nanotechnology* , 1 (2024).

[56] J. H. Muten, A. J. Copeland, and E. McCann, *Physical Review B* **104**, 035404 (2021).

[57] B. Pamuk, J. Baima, F. Mauri, and M. Calandra, *Physical Review B* **95**, 075422 (2017).

[58] Z. Lu, T. Han, Y. Yao, A. P. Reddy, J. Yang, J. Seo, K. Watanabe, T. Taniguchi, L. Fu, and L. Ju, *Nature* **626**, 759 (2024).

[59] Z. Lu, T. Han, Y. Yao, Z. Hadjri, J. Yang, J. Seo, L. Shi, S. Ye, K. Watanabe, T. Taniguchi, *et al.*, *Nature* , 1 (2025).

[60] Y. Cao, V. Fatemi, S. Fang, K. Watanabe, T. Taniguchi, E. Kaxiras, and P. Jarillo-Herrero, *Nature* **556**, 43 (2018).

[61] M. Yankowitz, S. Chen, H. Polshyn, Y. Zhang, K. Watanabe, T. Taniguchi, D. Graf, A. F. Young, and C. R. Dean, *Science* **363**, 1059 (2019).

[62] X. Lu, P. Stepanov, W. Yang, M. Xie, M. A. Aamir, I. Das, C. Urgell, K. Watanabe, T. Taniguchi, G. Zhang, A. Bachtold, A. H. MacDonald, and D. K. Efetov, arXiv preprint arXiv:1903.06513 (2019).

[63] J. M. Park, Y. Cao, K. Watanabe, T. Taniguchi, and P. Jarillo-Herrero, *Nature* **590**, 249 (2021).

[64] Z. Hao, A. Zimmerman, P. Ledwith, E. Khalaf, D. H. Najafabadi, K. Watanabe, T. Taniguchi, A. Vishwanath, and P. Kim, *Science* **371**, 1133 (2021).

[65] X. Liu, N. Zhang, K. Watanabe, T. Taniguchi, and J. Li, *Nature Physics* **18**, 522 (2022).

[66] M. Sammon, X. Fu, Y. Huang, M. A. Zudov, B. I. Shklovskii, G. C. Gardner, J. D. Watson, M. J. Manfra, K. W. Baldwin, L. N. Pfeiffer, *et al.*, *Physical Review B* **100**, 241303 (2019).

[67] T. Han, Z. Lu, Y. Yao, J. Yang, J. Seo, C. Yoon, K. Watanabe, T. Taniguchi, L. Fu, F. Zhang, *et al.*, *Science* **384**, 647 (2024).

[68] Y. Sha, J. Zheng, K. Liu, H. Du, K. Watanabe, T. Taniguchi, J. Jia, Z. Shi, R. Zhong, and G. Chen, *Science* **384**, 414 (2024).

## METHODS

In this section, we provide detailed discussions to further substantiate the results presented in the main text. Our focus is on the direct connection between time-reversal and rotational symmetry breaking, supported by a comprehensive characterization of magnetic-hysteresis measurement across the low-temperature phase space. Additionally, we elaborate on the extraction of intrinsic anisotropy from the conductivity matrix and discuss the subtleties of interpreting angle-resolved transport data in the presence of stripe order, particularly under conditions of extreme anisotropy.

### I. Direct link between anomalous Hall effect and transport anisotropy

A recent study on rhombohedral hexalayer graphene reports that the emergence of the anomalous Hall effect is directly linked to a nematic transition [21]. Here, we show that a similar correlation arises in the high- $D$  regime, where the anomalous Hall effect occurs within regions of the  $n$ - $D$  phase space characterized by extreme transport anisotropy.

Figure M1a displays a color map of the transport anisotropy, defined as  $\xi = (R_{\max} - R_{\min})/(R_{\max} + R_{\min})$ , plotted as a function of carrier density  $n$  and displacement field  $D$ . Regions of strong anisotropy, highlighted in red, appear prominently in the high- $D$  regime surrounding the SC *i* and SC *ii* phases.

Figures M1b–j present magnetic hysteresis loops measured at various  $n$  and  $D$  values, revealing a clear correlation between the anomalous Hall effect and anisotropic transport.

At locations marked by open blue circles in Fig. M1a, the transport response exhibits pronounced magnetic hysteresis (Figs. M1b–f), coinciding with strong anisotropy.

In contrast, at the points marked by open red diamonds, angle-resolved measurements reveal suppressed anisotropy and an absence of anomalous Hall response (Fig. M2).

### II. Angle-resolved transport measurement in the linear response regime

To perform angle-resolved transport measurements using a sunflower sample geometry, two configurations— $R_{\parallel}$  and  $R_{\perp}$ —are commonly employed, as illustrated in Fig. M3 [21, 24–27]. As a function of the angle  $\phi$ , both the longitudinal ( $R_{\parallel}$ ) and transverse ( $R_{\perp}$ ) resistances exhibit two-fold angular oscillations, described by:

$$R_{\parallel}(\phi) = R_0 - \Delta R \cos 2(\phi - \alpha), \quad (M1)$$

$$R_{\perp}(\phi) = R_H + \Delta R \sin 2(\phi - \alpha), \quad (M2)$$

where  $\Delta R$  is the oscillation amplitude,  $R_0$  is the mean value of  $R_{\parallel}$ ,  $R_H$  is the average of  $R_{\perp}$ , and  $\alpha$  denotes the principal axis direction corresponding to the maximum conductivity. According to theoretical analysis [24], Eqs. (1) and (2) fully define the linear-response conductivity matrix. The ratio  $\Delta R/R_0$ , equivalent to the anisotropy parameter  $\xi$  in Fig. 2b, provides a quantitative measure of anisotropy strength. A non-zero  $R_H$  reflects antisymmetric off-diagonal elements in the conductivity matrix, corresponding to an anomalous Hall effect arising from orbital ferromagnetism [21].

### III. Actual anisotropy in conductivity

Previous theoretical and experimental studies have established a robust framework for extracting the full conductivity matrix from angle-resolved transport measurements [24, 25]. In regimes of moderate anisotropy, the resistance ratio  $R_{\max}/R_{\min}$ —determined from  $R_{\parallel}$  with current applied along two principal axes—closely approximates the intrinsic conductivity ratio  $\sigma_{\max}/\sigma_{\min}$ . However, under conditions of extreme anisotropy, this equivalence breaks down:  $R_{\max}/R_{\min}$  becomes significantly influenced by sample geometry and non-uniform potential distribution, leading to deviations from the true conductivity ratio.

A theoretical framework introduced in Ref. [24] enables quantitative extraction of intrinsic conductivity anisotropy using the sunflower geometry. This method determines the potential distribution along the sample perimeter for a given conductivity tensor, allowing one to map between the measured resistance ratio  $R_{\max}/R_{\min}$  and the underlying conductivity ratio  $\sigma_{\max}/\sigma_{\min}$ .

As an illustration, Fig. M4 shows calculated potential distributions across the sample disk for different source-drain configurations, assuming an intrinsic conductivity anisotropy of  $\sigma_{\max}/\sigma_{\min} = 5$ . When current flows along the axis of maximum conductivity, the potential tends to fan out in the transverse direction due to the anisotropic conductivity tensor. This causes voltage probes aligned with the current path to underestimate the true voltage drop, leading to an inflated value of the measured resistance ratio. In this example, the resulting resistance anisotropy is  $R_{\max}/R_{\min} = 16.5$ , more than three times larger than the actual conductivity ratio.

Using this method, we re-examine the resistance data in Fig. 2a–b to extract the intrinsic conductivity anisotropy from the measured values of  $R_{\max}$  and  $R_{\min}$ . Figure M5a plots the temperature dependence of the normalized anisotropy  $\Delta\sigma/\bar{\sigma}$ , where  $\bar{\sigma} = (\sigma_{\max} + \sigma_{\min})/2$  and

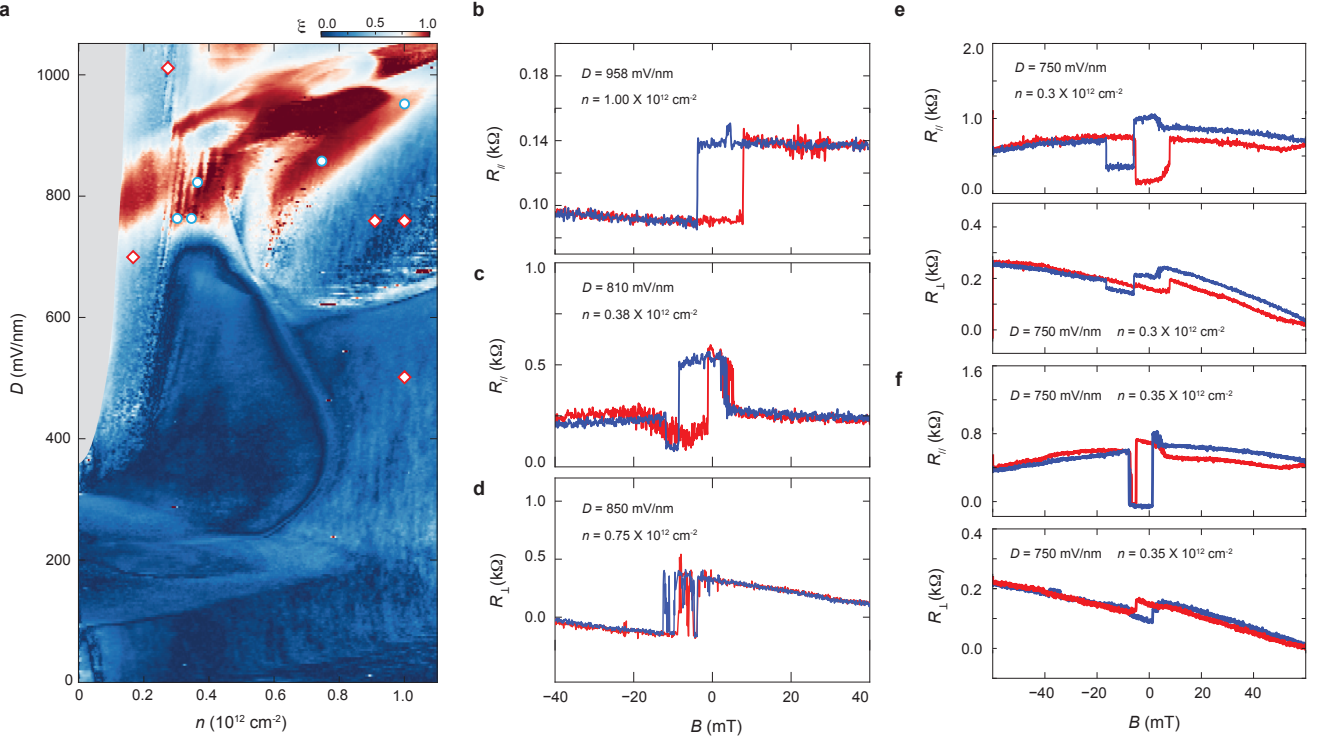


**FIG. M1. Evolution of anisotropy and anomalous Hall effect across the low-temperature phase diagram.** (a) Color map of the anisotropy parameter  $\xi = (R_{\max} - R_{\min})/(R_{\max} + R_{\min})$  plotted as a function of carrier density  $n$  and displacement field  $D$ . Regions of extreme anisotropy are shown in red on the chosen color scale, while blue and dark blue indicate more isotropic transport responses. (b–f) Transport responses measured at different  $n$  and  $D$  values as an out-of-plane magnetic field is swept back and forth. Magnetic hysteresis loops, indicative of orbital ferromagnetism, are observed in regimes exhibiting strong transport anisotropy, marked by blue open circles. By contrast, regions with weaker anisotropy in panel (a), marked by red open diamonds, show no magnetic hysteresis as demonstrated in Fig. M2.

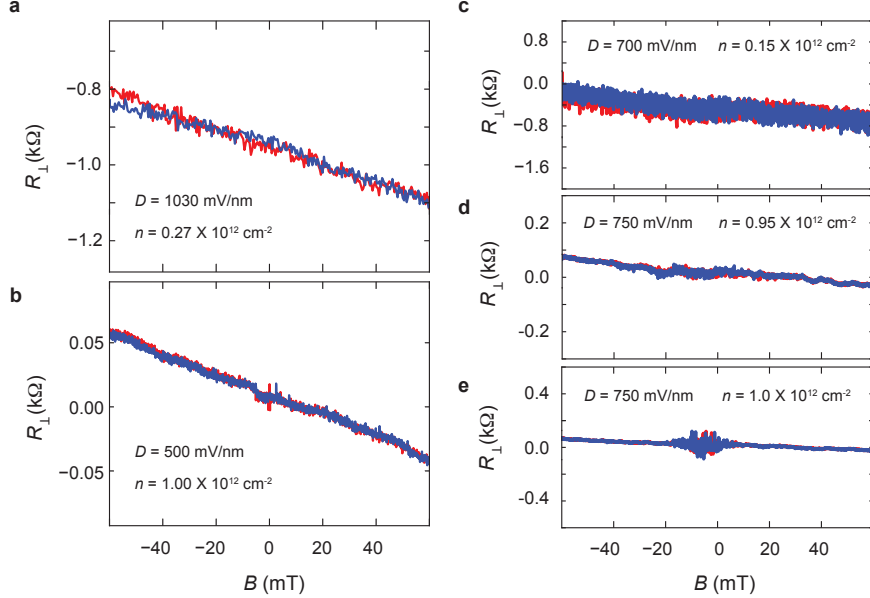


**FIG. M2. Absence of magnetic hysteresis in isotropic regions.** Transport responses measured at different  $n$  and  $D$  values as an out-of-plane magnetic field is swept back and forth. These measurements correspond to the red open diamonds in Fig. M1a, which indicate regions of weaker anisotropy and show no magnetic hysteresis.

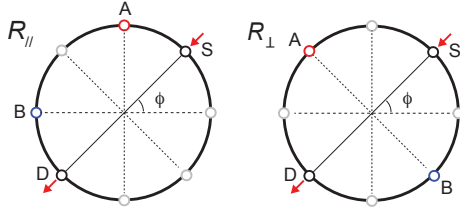


FIG. M3. Angle-resolved transport measurement with the “sunflower” sample geometry Schematic of the angle-resolved transport measurement setup used to extract  $R_{\parallel}$  (left) and  $R_{\perp}$  (right) in a sample shaped into the so-called “sunflower” geometry.

$\Delta\sigma = (\sigma_{\max} - \sigma_{\min})/2$ . This quantity is directly related to  $\xi$  and  $\Delta R/R_0$ , and provides a geometry-independent measure of the intrinsic anisotropy encoded in the conductivity tensor.

Figure M5b presents the temperature evolution of the conductivity ratio  $\sigma_{\max}/\sigma_{\min}$ . A sharp cusp near  $T = 1.5$  K marks the onset of the nematic transition, with  $\sigma_{\max}/\sigma_{\min} \approx 8$ . This level of anisotropy is comparable to that found in quantum Hall stripe phases, which typically exhibit intrinsic anisotropy ratios in the range of 20–40 [66].

Below 1 K, the ratio  $\sigma_{\max}/\sigma_{\min}$  diverges due to the onset of superconductivity. Because the superconducting and stripe orders emerge nearly simultaneously, disentangling their respective contributions to the low-temperature anisotropy remains a significant challenge.

A unique opportunity to isolate the intrinsic anisotropy of the stripe phase arises when superconductivity is suppressed by an out-of-plane magnetic field. Figure M6 shows the temperature dependence of  $\xi$ , calculated from the values of  $R_{\max}$  and  $R_{\min}$  in Fig. 4g–i, under different values of  $B_{\perp}$ . In the superconducting regime,  $\xi$  approaches unity, reflecting a diverging conductivity ratio  $\sigma_{\max}/\sigma_{\min}$ . Above the superconducting transition, however,  $\xi$  serves as a reliable measure of the intrinsic anisotropy.

Notably,  $\xi$  decreases with increasing magnetic field. At zero field, it exhibits a pronounced cusp at the nematic transition temperature  $T_{\text{nem}}$ , corresponding to  $R_{\max}/R_{\min} \approx 25$  and an intrinsic conductivity ratio of  $\sigma_{\max}/\sigma_{\min} \approx 7$ . In contrast, at  $B = -1$  T,  $\xi$  becomes largely temperature-independent below 2.5 K, yielding  $R_{\max}/R_{\min} \approx 12$  and  $\sigma_{\max}/\sigma_{\min} \approx 6$ .

The observation in Fig. M6 suggests that the emergence of stripe order is closely linked to the stability of the superconducting phase. Understanding how the stripe order and the nematic transition evolve with  $B_{\perp}$  remains an important open question. Such insight will be critical for evaluating the intrinsic anisotropy of the stripe phase in the zero-field limit.

#### IV. SC *i* and SC *ii* regimes

The emergence of stripe order is a universal feature across the entire parameter space of the SC *i* phase. When current flows perpendicular to the stripes, a highly resistive transport response is observed (middle panel of Fig. M7), signaling the apparent absence of superconductivity in this configuration. This behavior stands in stark contrast to the vanishing  $R_{\parallel}$  observed when current is applied parallel to the stripe orientation (left middle panel of Fig. M7). The anisotropic nature of the SC*i* phase is further highlighted by line cuts taken at fixed displacement field  $D$  (top panels of Fig. M8).

Even when current is applied transverse to the stripe direction,  $R_{\perp}$  drops to zero within the SC *i* region (right panel of Fig. M7, bottom panels of Fig. M8). This observation is consistent with superconductivity developing exclusively along the stripes, which equalizes the potential along their direction, thus resulting in a vanishing  $R_{\perp}$  despite a finite, resistive  $R_{\parallel}$ . Moreover, the extreme anisotropy appears to be unique to the SC *i* phase. Fig. M9 shows the transport response measured along a diagonal line crossing both the SC *i* and SC *ii* phases. While  $R_{\parallel}$  exhibits a pronounced discrepancy between the directions parallel and perpendicular to the stripe order in SC *i*, this discrepancy vanishes in SC *ii*.

In the  $n$ - $D$  region surrounding the SC*i* phase, the principal axis aligns with  $\phi = 135^\circ$  (see Fig. 1d). Therefore, a non-zero  $R_{\perp}$  measured along  $\phi = 135^\circ$  indicates a finite anomalous Hall coefficient in this regime. The right panel of Fig. M7 shows  $R_{\perp}$ , revealing that both the SC*i* phase is embedded within a broader region exhibiting a robust anomalous Hall effect.

#### V. Insulating and superconducting responses

Within the SC *i* phase, both insulating and superconducting behaviors are observed, depending on the measurement configuration. These responses reflect the strong transport anisotropy imposed by the stripe charge order.

*Insulating Behavior.* Insulating transport is observed in the following configurations:

- When current flows perpendicular to the stripe orientation,  $R_{\parallel}$  shows insulating behavior at low temperatures (Fig. M10a, c, d).
- When current flows at an angle to the stripe orientation—such as  $\phi = 270^\circ$ —the voltage response measured perpendicular to the stripes exhibits insulating behavior (Fig. M10a).

*Superconducting Behavior.* Superconducting transport, characterized by vanishing resistance, is observed under the following conditions:

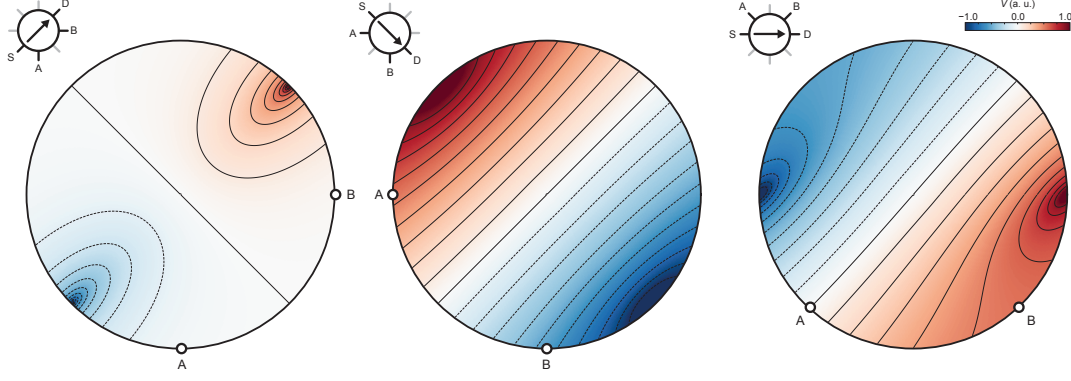


**FIG. M4. Potential distribution across a disk-shaped sample in the presence of extreme anisotropy.** Simulated potential distribution across a disk-shaped sample with different source and drain configurations, assuming an intrinsic conductivity anisotropy of  $\sigma_{\max}/\sigma_{\min} = 5$ , where  $\sigma_{\max}$  and  $\sigma_{\min}$  represent the conductivities along the two principal axes of the underlying electronic order. This potential distribution enables the extraction of  $R_{\parallel}$  from angle-resolved transport measurements. For current applied along  $\phi = 225^\circ$  (left) and  $\phi = 135^\circ$  (right), the calculated resistance ratio is  $R_{\max}/R_{\min} = 16.5$ .

- When current flows parallel to the stripe orientation,  $R_{\parallel}$  shows superconducting behavior at low temperatures (Fig. M11a).
- When current flows at an angle to the stripe orientation, such as  $\phi = 270^\circ$ , the voltage response measured parallel to the stripe direction exhibits superconducting behavior (Fig. M11c).
- Under the same angled configuration ( $\phi = 270^\circ$ ),

$R_{\parallel}$  also shows superconducting behavior, although with a reduced  $T_c$  (Fig. M11b).

These observations underscore the intrinsic one-dimensional nature of superconductivity in the *SC i* phase and the critical role of stripe orientation in defining transport response.

The observation of superconducting behavior in  $R_{\parallel}$  along  $\phi = 270^\circ$  is particularly noteworthy. In this config-

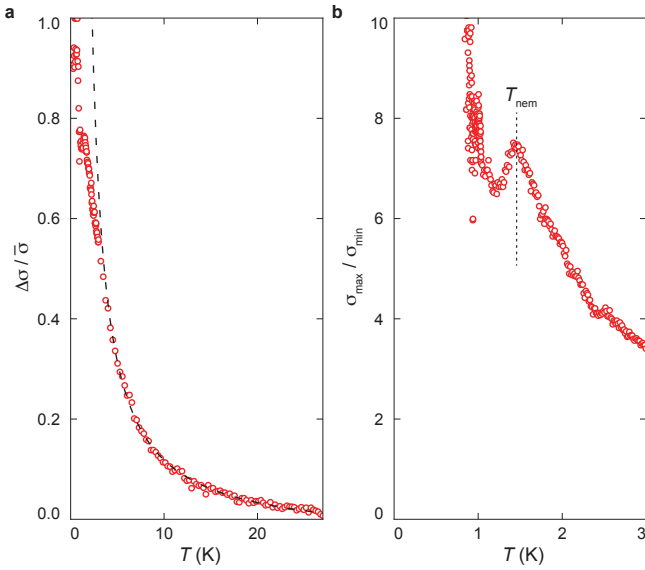


**FIG. M5. Temperature dependence of anisotropy.** (a) Temperature dependence of  $\Delta\sigma/\bar{\sigma}$  in the metallic phase, exhibiting Curie-Weiss-like behavior characteristic of nematic fluctuations. (b) Temperature dependence of the anisotropy ratio  $\sigma_{\max}/\sigma_{\min}$  in the low-temperature regime. The rapid divergence below  $T = 1$  K signals the onset of stripe-ordered superconductivity. Both quantities are extracted from the angle-resolved transport data shown in Fig. 2a–b.

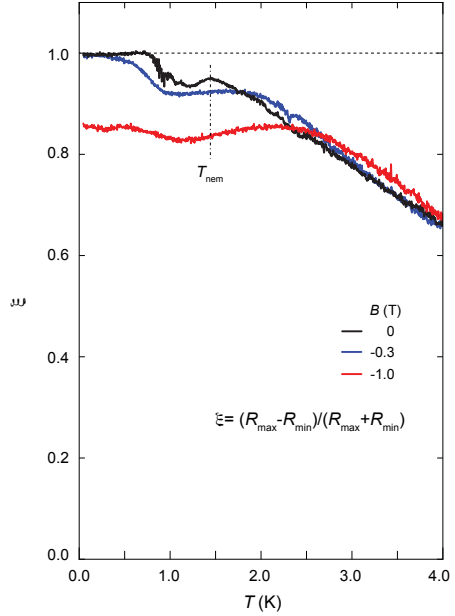


**FIG. M6. Temperature dependence of resistance ratio in the presence of  $B$ .**  $\xi$  as a function of temperature measured at different values of  $B$ . The measurements are performed at  $D = 958$  mV/nm and  $n = 8.0 \times 10^{12} \text{ cm}^{-2}$ . Vertical dash-dotted line marks the nematic transition temperature  $T_{\text{nem}}$  at  $B = 0$ , which is identified in Fig. 3.

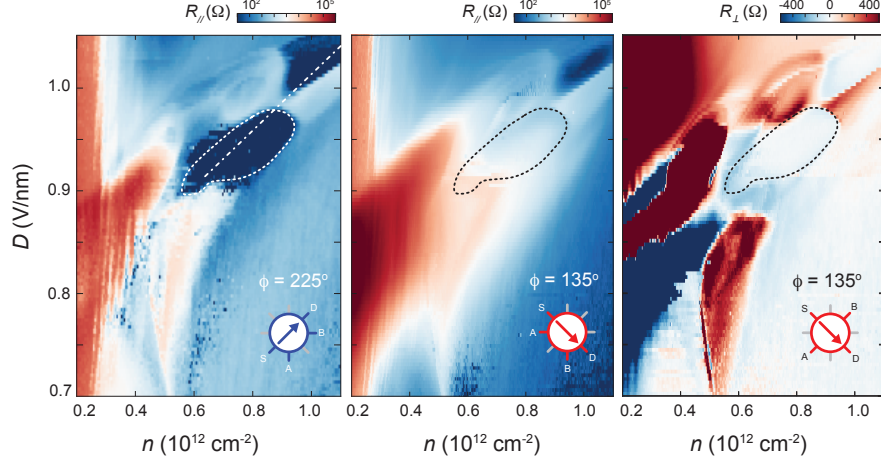


FIG. M7. **SC *i* and SC *ii* regimes.** Color map of  $R_{\parallel}$  at  $\phi = 225^\circ$  (left, along the stripe orientation),  $R_{\parallel}$  at  $\phi = 135^\circ$  (middle, perpendicular to the stripe orientation), and  $R_{\perp}$  at  $\phi = 135^\circ$  (right, perpendicular to the stripe orientation), measured as a function of  $n$  and  $D$  around the SC *i* and SC *ii* regimes.

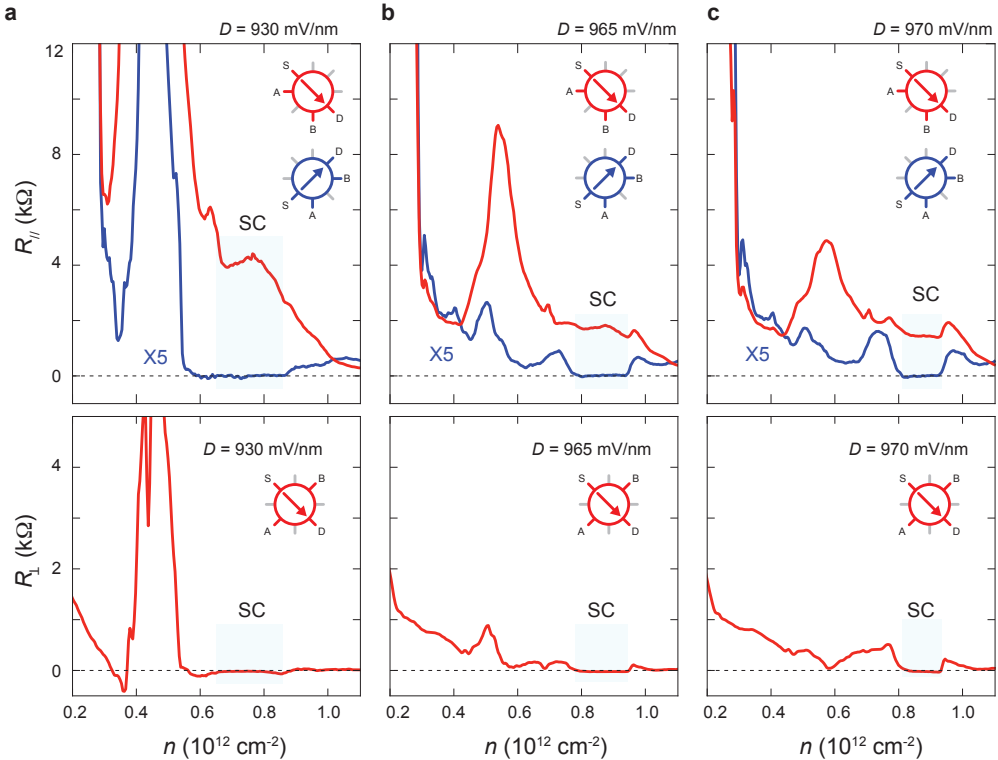


FIG. M8. **Density line cuts across the SC *i* phase.** Line cuts taken at fixed displacement fields from the  $n$ - $D$  maps in Fig. M7, shown for (a)  $D = 0.93$  V/nm, (c)  $D = 0.965$  V/nm, and (d)  $D = 0.97$  V/nm. The top panels show  $R_{\parallel}$ , and the bottom panels show  $R_{\perp}$ . The blue trace is multiplied by a factor of 5 for clarity.

uration, the voltage response is measured across multiple stripes, as illustrated in the inset of Fig. M11b. The vanishing  $R_{\parallel}$  in this scenario could originate from two possible mechanisms: (i) adjacent stripes are coherently coupled via Josephson tunneling, enabling phase coherence across stripes and resulting in zero resistance when mea-

sured perpendicular to their orientation; (ii) the stripe pattern forms local domains that happen to connect contacts A and B in this particular geometry, enabling superconducting paths along irregular orientations.

Both interpretations reflect the complex spatial structure of superconductivity in the SC *i* phase and highlight

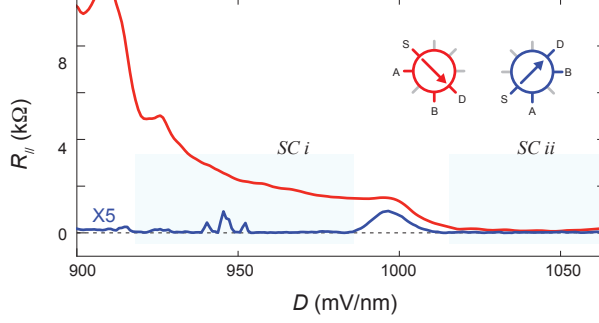


FIG. M9. **Across  $SC\ i$  and  $SC\ ii$  regimes.** Longitudinal resistance  $R_{\parallel}$  measured along the diagonal dashed line shown in Fig. M7a, traversing both superconducting pockets  $SC\ i$  and  $SC\ ii$ .

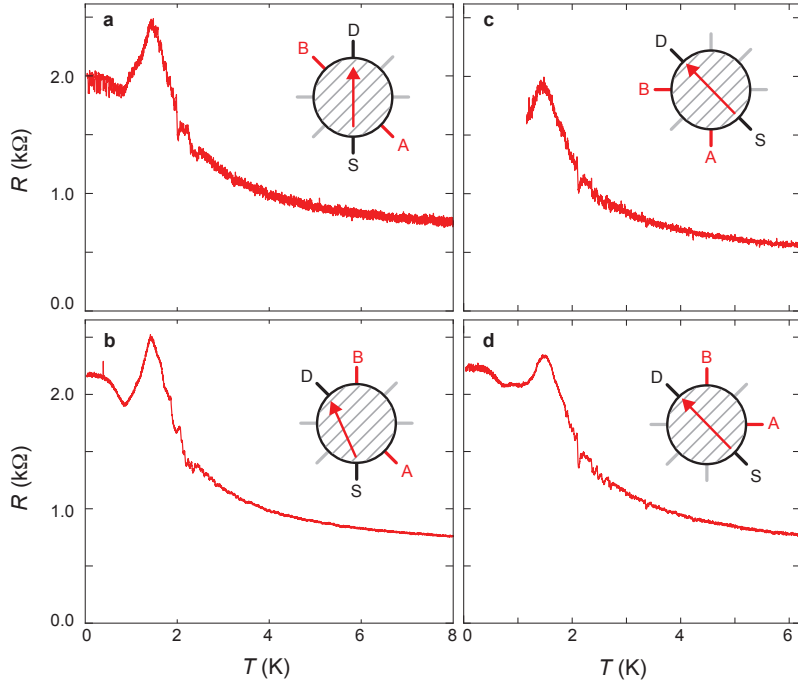


FIG. M10. **Configurations with insulating behaviors.** Insulating response is observed between contacts aligned perpendicular to the stripe orientation. Current does not need to flow perpendicular to the stripes to generate the insulating behavior, as demonstrated by panel (a) and (b).

the role of stripe domain configuration in determining transport behavior.

Notably, measurements performed perpendicular to the stripe orientation consistently exhibit a distinctive low-temperature cusp in resistance (Fig. M10). A plausible origin of this resistance cusp is the onset of stripe charge order. The highest superconducting transition temperature ( $T_c$ )—measured with current flowing parallel to the stripes—emerges consistently just below stripe formation. This observation strongly suggests that superconductivity develops directly from the pre-existing stripe-ordered state.

## VI. Angular interplay between superconducting and metallic phases

Recent work has shown that superconductivity in magic-angle twisted trilayer graphene exhibits a distinctive angular interplay with the metallic phase above the superconducting transition [27]. Specifically, the most robust superconducting response—characterized by the highest critical current and transition temperature—emerges along the direction of maximum resistivity (i.e., minimum conductivity) in the metallic state.

In contrast, the  $SC\ i$  phase displays the opposite angular correlation. Due to the emergence of stripe order, superconducting transport is confined along the direction

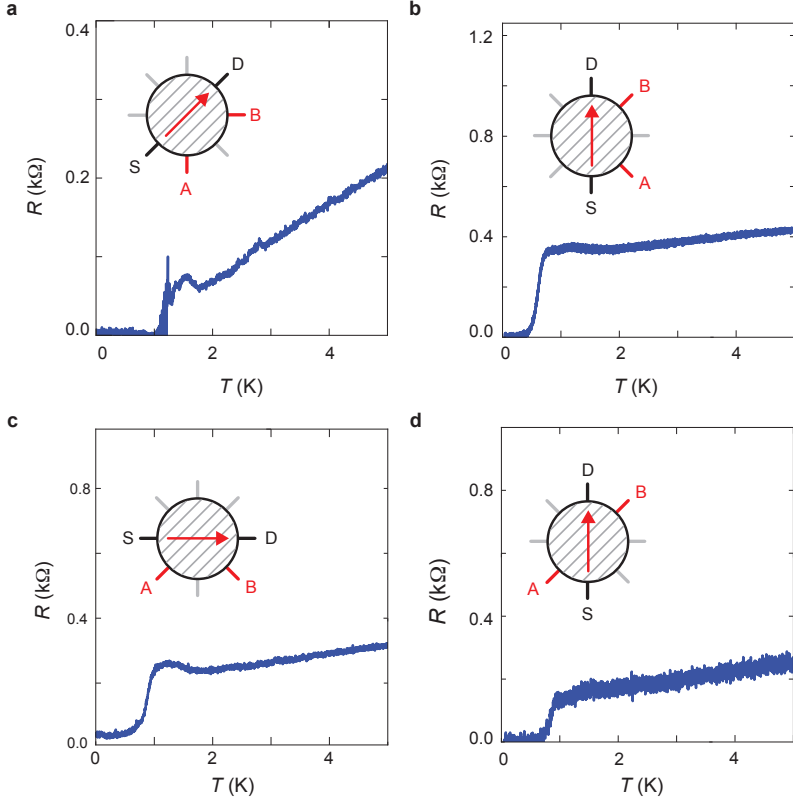


FIG. M11. **Configurations with superconducting behaviors.** The superconducting transition temperature, defined by the temperature where resistance vanishes to zero, is highly dependent on the direction of current flow, as well as the direction of measurement.

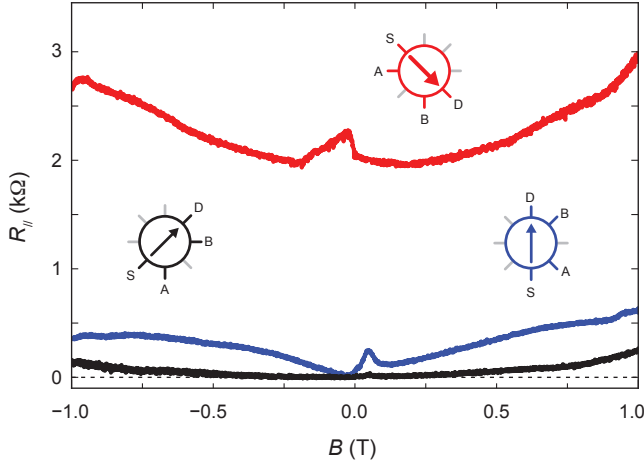


FIG. M12. **Dependence on  $B_{\perp}$ .**  $R_{\parallel}$  as a function of  $B_{\perp}$  measured with current being applied along different directions.

of maximum conductivity in the metallic state above the superconducting transition temperature.

Interestingly, although  $SCii$  and  $SCiii$  do not exhibit clear signatures of stripe order, they follow the same angular correlation as  $SCi$ —with superconductivity pref-

entially developing along the direction of highest conductivity in the normal state.

Figure M13 illustrates this angular interplay by comparing the angular dependence of the critical supercurrent  $I_c$ —defined by the position of maximum  $dV/dI$  in the I-V characteristics—with the transport anisotropy of the metallic phase. Anisotropy in the metallic state is characterized by the angular dependence of  $R_{\parallel}$  and  $R_{\perp}$ . Fitting the data using Eqs. M1–M2 reveals two principal axes: the direction of minimum resistivity (maximum conductivity), marked by the vertical green dashed line, and the direction of maximum resistivity, marked by the gray dashed line. As shown in Fig. M13d, the maximum  $I_c$  aligns with the direction of maximum conductivity, while the minimum  $I_c$  occurs along the direction of minimum conductivity.

According to theoretical arguments based on a simple Ginzburg–Landau framework, this angular behavior is consistent with a uniform superconducting gap and an anisotropic effective mass. Notably, this rules out order parameter structures involving a mixture of  $s$ - and  $d$ -wave components but remains consistent with a pure  $s$ -wave symmetry or certain  $p$ -wave states [27].

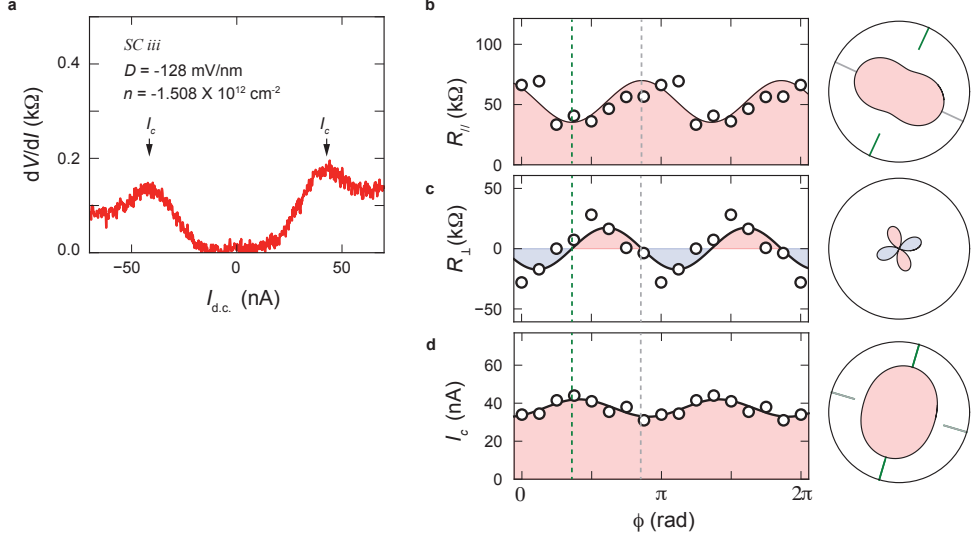


FIG. M13. **The angular dependence of SC *iii*.** (a) I-V characteristics measured from *SC iii*. Critical current  $I_c$  is defined by the peak position in the differential resistance  $dV/dI$ . (b-c) Angular dependence of  $R_{\parallel}$  and  $R_{\perp}$  measured from the normal state at  $T = 1.5$  K and the same  $n$  and  $D$  as panel (a). Black solid line is the best fit to data using Eq. M1-2. (d) Angular dependence of  $I_c$ . Green vertical dashed line mark the direction of maximum conductivity (minimum resistivity) in the normal state, which corresponds to the direction of maximum  $I_c$  in the superconducting phase.

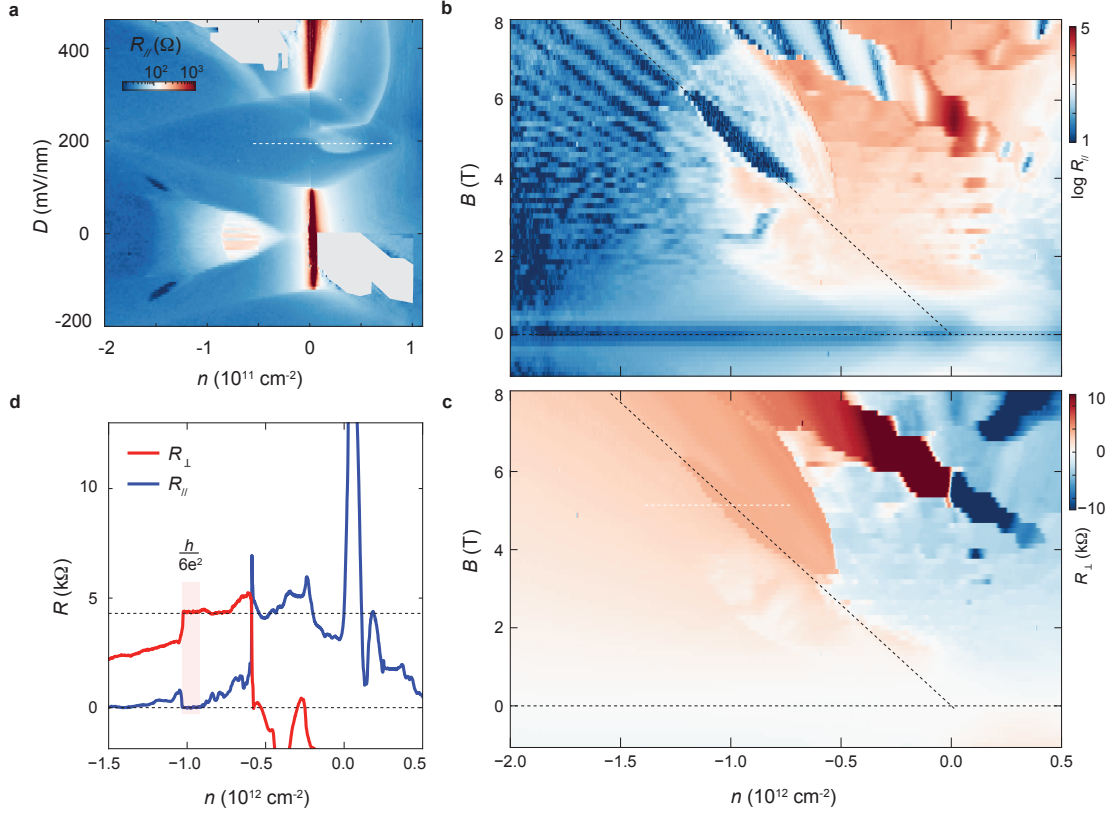


FIG. M14. **Identification of rhombohedral hexalayer.** (a) Color scale map of  $R_{\parallel}$  measured as a function of  $n$  and  $D$ . The white dashed line cuts across the anomalous Hall effect regime near  $D = 200$  mV/nm. Color scale map of (b)  $R_{\parallel}$  and (c)  $R_{\perp}$  as a function of  $n$  and  $B$ , taken at the  $D$  value corresponding to the white dashed line in panel (a). (c)  $R_{\parallel}$  and  $R_{\perp}$  as a function of  $n$ , measured along the white dashed line in panel (c). The observed plateau in  $R_{\perp}$  coinciding with vanishing  $R_{\parallel}$ , points to rhombohedral stacking hexalayer graphene.

## VII. Rhombohedral hexalayer graphene

Figure M14 determines the layer number of the rhombohedral sample by extracting the Chern number of a valley-polarized state that emerges near charge neutrality, close to the layer-polarization transition (Fig. M14a). Previous studies have established that the Chern number of this state is directly correlated with the number of layers in rhombohedral graphene [67, 68].

The extracted Chern number, together with the observed transport responses, confirms that the sample is rhombohedral hexalayer graphene.

## SUPPLEMENTARY MATERIALS

## Superconductivity, Anomalous Hall Effect, and Stripe Order in Rhombohedral Hexalayer Graphene

Erin Morissette\*, Peiyu Qin\*, Hai-Tian Wu, Naiyuan James Zhang, Kenji Watanabe, Takashi Taniguchi, and J.I.A. Li<sup>†</sup>

<sup>†</sup> Corresponding author. Email: jia.li @brown.edu

### I. The impact of angular sequence on magnetic hysteresis loops

A sequential measurement that rotates through different current flow directions has a striking effect on first-order transitions. Here, we investigate the impact of such a protocol on the magnetic hysteresis transition, using the same rhombohedral hexalayer graphene sample. Figure S1a shows the magnetic hysteresis loop obtained using a fixed measurement configuration, as the out-of-plane magnetic field is swept back and forth. The observed hysteresis arises from the formation of magnetic domains and the finite energy barrier associated with domain wall motion.

In contrast, Fig. S1b shows the Hall coefficient measured using a sequential scheme, where the current direction is rotated through multiple angles at each magnetic field value. Remarkably, this angular rotation suppresses the magnetic hysteresis, effectively collapsing the forward and reverse  $B$ -sweep curves onto a single trajectory.

These results suggest that angularly sequential measurements significantly influence magnetic domain wall dynamics, possibly by preventing domain wall pinning or facilitating relaxation toward the equilibrium ground state. Consequently, this measurement approach provides a powerful tool for probing equilibrium behavior across first-order magnetic transitions.

This finding also sheds new light on the sequential measurements shown in Fig. S2c, where a similar protocol leads to a marked suppression of the superconducting transition temperature. The results raise the possibility that angular current rotation dramatically alters the domain structure of the stripe order, thereby strongly impacting the superconducting transition.

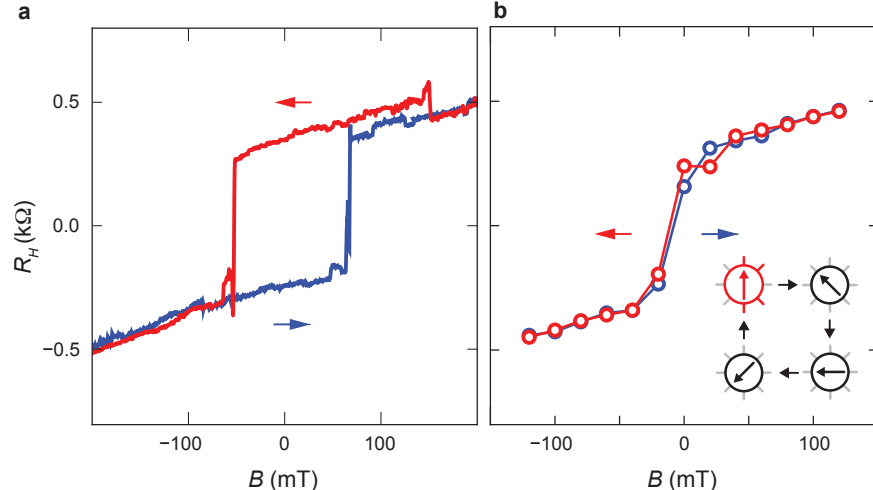
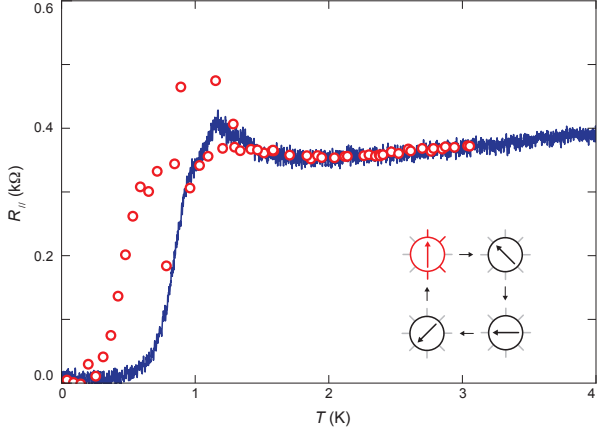


FIG. S1. The impact of angular sequence on first order transitions. (a)  $R_H$  measured at fixed  $n$  and  $D$  in the multiferroic state, as an out-of-plane magnetic field  $B$  is swept back and forth, showing clear magnetic hysteresis. (b) Sequential measurement performed at the same  $n$  and  $D$  values as in panel (a), where all current directions are cycled through before  $B$  is ramped to the next value. The angular sequence suppresses the hysteresis, collapsing the forward and reverse  $B$  sweeps onto a single curve.



**FIG. S2. Angular control of the superconducting transition.**  $R$ - $T$  curves of the  $SC\ i$  phase measured on warming. Open red circles represent data obtained using a sequential angular protocol:  $R_{\parallel}$  is measured with an a.c. current of 4nA applied along  $\phi = 270^\circ$ , while between consecutive measurements, current is sequentially rotated through  $\phi = 135^\circ, 180^\circ$ , and  $225^\circ$  (illustrated in the bottom-right inset). The dark blue trace corresponds to continuous measurements without configuration switching and is identical to the reference curve shown in Fig. S3a. While configuration switching has negligible impact at higher temperatures, it induces significant hysteretic variations in the transport response near the superconducting transition.

## II. The impact of angular sequence on superconducting transitions

The most pronounced variation in  $T_c$  is induced by a specific measurement sequence, wherein an a.c. current of 3nA is sequentially applied along directions  $\phi = 135^\circ, 180^\circ, 225^\circ$ , and  $270^\circ$ . During this sequence, the transport response ( $R_{\parallel}$ ) is measured exclusively at  $\phi = 270^\circ$  (red open circles in Fig. 3c) and compared against a reference  $R$ - $T$  curve (blue trace), taken from Fig. S3a, which corresponds to continuous measurements performed without changing the current direction.

While the configuration switching has negligible influence at higher temperatures, it induces a marked suppression of the superconducting transition temperature  $T_c$ , as well as enhanced variability in  $R_{\parallel}$  near  $T = 1$  K. These fluctuations reflect abundant switching events in the transport response, suggestive of a dynamic reconfiguration of the underlying electronic order.

Although the impact of sequential measurements has not been extensively explored in prior studies, its pronounced effect here is striking. A plausible explanation is that the sequential current reorients the stripe order—consistent with the strong dependence of  $T_c$  on current direction shown in Fig. 2a. This provides further evidence that the superconducting transition is intimately tied to the orientation of the stripe phase.

Further evidence of this tunability emerges in the form of current-driven switching observed in the I-V characteristics. As shown in Fig. S4, the differential resistance  $dV/dI$  displays numerous current-induced transitions at low  $B_{\perp}$ , appearing as discontinuous jumps or fluctuations in the signal. These features are largely suppressed once  $B_{\perp}$  exceeds 0.1 T, highlighting the sensitivity of the superconducting state to both current direction and applied magnetic field.

## III. Hysteresis across the superconducting transition on warming

Hysteretic behaviors are observed across the temperature-driven superconducting transition. Figure S3 shows  $R$ - $T$  curves from five consecutive measurements, all performed at identical carrier density ( $n$ ), displacement field ( $D$ ), and using the same warming rate. While the curves exhibit highly reproducible behavior at elevated temperatures, they bifurcate distinctly below the temperature marked by the vertical dashed line, which corresponds to the resistance cusp associated with the nematic transition. This bifurcation results in clearly separated superconducting transitions.

These variations reveal different forms of hysteresis in the  $R$ - $T$  characteristics: (i) changes in the superconducting transition temperature  $T_c$ ; and (ii) the appearance or absence of a resistance peak above  $T_c$ . While the exact nature of these hysteretic effects remains an open question, they could arise from two possible mechanisms.

First, the hysteresis may originate from the nematic transition itself. As shown in previous angle-resolved measurements in graphene moiré systems [27], temperature cycling can introduce variations in the underlying transport anisotropy, which in turn may lead to fluctuations in the superconducting transition temperature.

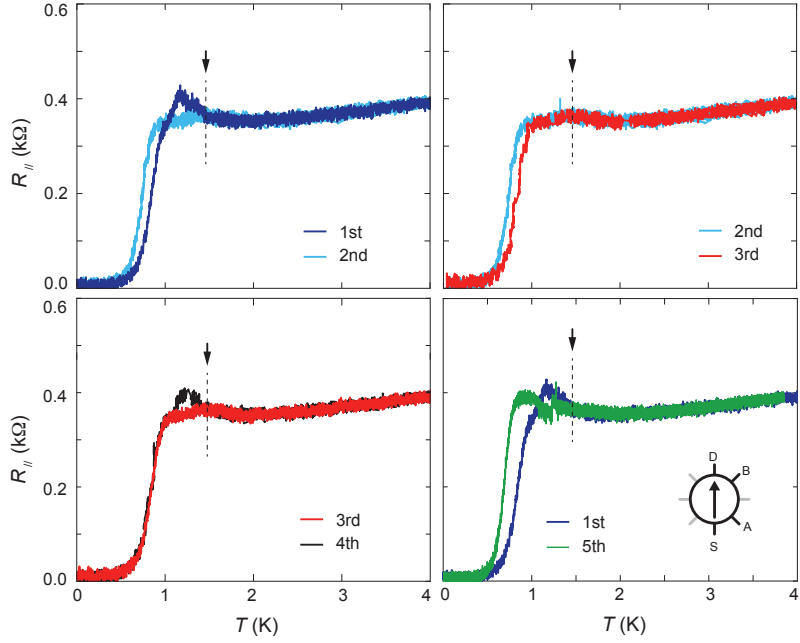


**FIG. S3. Hysteresis near the superconducting transition on warming.**  $R$ - $T$  curves from four consecutive measurements, all performed at identical carrier density ( $n$ ), displacement field ( $D$ ), and using the same warming rate. The traces exhibit several distinct forms of hysteresis: shifts in the superconducting transition temperature ( $T_c$ ), the presence or absence of a resistance peak just above  $T_c$ , and discontinuous jumps in the  $R$ - $T$  curve (green trace in the bottom right panel).

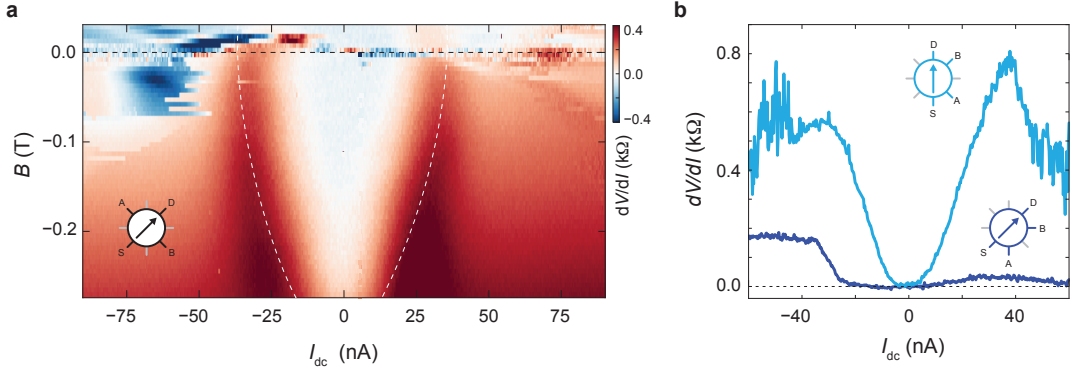


**FIG. S4. Current-voltage characteristic of the  $SC$   $i$  phase.** (a) Color scale map of differential resistance measured as a function of d.c. current bias and out-of-plane magnetic field. The measurement is performed at  $n = 0.8 \times 10^{12} \text{ cm}^{-2}$  and  $D = 958 \text{ mV/nm}$ , with current flowing along the stripe orientation. (b)  $dV/dI$  as a function of d.c. current measured at  $B = 0$  with different  $\phi$ .

Second, the hysteresis observed upon warming could be connected from the process of stripe formation. In this scenario, subtle changes in the stripe configuration between successive temperature cycles could be responsible for the observed variations in the superconducting transport response.